RSC Advances

This article can be cited before page numbers have been issued, to do this please use: H. Ma, Y. Su, C. Jiang and A. Nathan, *RSC Adv.*, 2016, DOI: 10.1039/C6RA18645A.

ROYAL SOCIETY OF CHEMISTRY

www.rsc.org/advances

View Article Online
DOI: 10.1039/C6RA18645A

RSC Advances

Inkjet-printed Ag electrodes on paper for high sensitivity impedance measurements

Received 00th January 20xx,
Accepted 00th January 20xx

DOI: 10.1039/x0xx00000x

www.rsc.org/

Hanbin Ma[a], Yang Su[a], Chen Jiang[a] and Arokia Nathan[a]

Low-cost electrodes were fabricated by standard office inkjet printer with commercial silver ink on glossy paper. Compared to conventional thin-film metal thermal evaporated gold electrodes, the paper-based ones show a two-order enhanced sensitivity for impedance measurement over low frequency range. The high surface roughness of paper electrodes increases the effective area of the electrolyte-electrode double layer capacitance, and therefore reduces the measured impedance at low frequency range. A passivation layer on the top of the paper electrodes is used to mimic the behaviour of the double layer capacitance. The surface roughness was characterized by optical microscope and atomic force microscopy. Finite element analysis and impedance equivalent model analysis were also performed for different thin-film electrode devices.

1 Introduction

Paper as a low-cost substrate has been widely used for disposable point-of-care diagnostic devices, and most of the advanced works have been summarised and compared in recent review papers[1–4]. Dedicated detection methods have also been developed, and these cover both optical-based techniques (fluorescent or colorimetric)[5,6] and electrochemical methods[7–9].

For all electrochemical methods, electrodes play a significant role as an interface between sensing system and analyte. There are a variety of fabrication techniques available to support different electrode material deposition and patterning. For example, vacuum-based thin-film deposition techniques (e.g. thermal/e-beam evaporation and metal sputtering) are the most reliable methods which provide access to noble metals e.g. gold and platinum, and they are used for most high-end applications[10–12]. On the other hand, printing techniques, such as screen and/or stencil printing, are more suitable for low-cost devices[1,3]. The frist carbon electrodes were screen-printed on paper for electrochemical detection by Dungchai et al.[7] in 2009. More materials, e.g. Ag/AgCl[13,14], CNT[15] and graphene[16], have become available for printing on paper via this technique. Ink-jet printing, using liquid phase conductive ink to replace the pastes in screen/stencil printing, is a promising technique that provides a "pattern on demand" feature[17]. However, the process requires printers normally equipped with sophisticated accessories, such as precise volume controlled nozzle and dedicated driving electronics. In addition, the ink composition and conductive particle selection also need to be carefully designed to increase the material printability[18,19]. In recent years, office inkjet printers compatible silver inks have been developed for fast circuit prototyping. Commercial suppliers (e.g. AgIC in this work) provide silver cartridges which enable regular office inkjet printer to print conductive silver tracks on glossy paper directly. This technique reduces the cost of inkjet printing significantly, and therefore can be utilised as an enabling technique for fabrication of disposable sensors.

In this work, we demonstrate the first time the possible use of office inkjet printing of silver electrodes on paper as ultra-sensitive electrodes for impedance measurement.

Impedance-based sensors, detecting and measuring samples-under-tests response under AC signals, have been gaining popularity for biological sensing in recent years[20]. These sensors are now widely applied in detections of various scales, e.g. DNA[21–23], proteins[24,25], cells[26,27] and bacteria[28]. For impedance-based measurements, an electrode-electrolyte double layer will be formed at the electrode surface, and this double layer capacitance behaves as a parasitic component to reduce the sensitivity[29]. In some measurements, it is also known as electrode polarisations, which significantly reduce sensing capability at low frequency (typically below 1 kHz). In recent years, novel-material-based electrodes with unique surface properties have been developed which could potentially address this problem, e.g. graphene, graphene related materials[30–32] and nanowires[33,34]. However, one of the major concerns about nanomaterials for

[a] Department of Engineering, Electrical Engineering Division, University of Cambridge, CB3 0FA, Cambridge UK
Electronic Supplementary Information (ESI) available: NaCl solution electrical parameters used for FEA in this work; Impeance equivalent model fitting and extracted paramters. See DOI: 10.1039/x0xx00000x

View Article Online
DOI: 10.1039/C6RA18645A

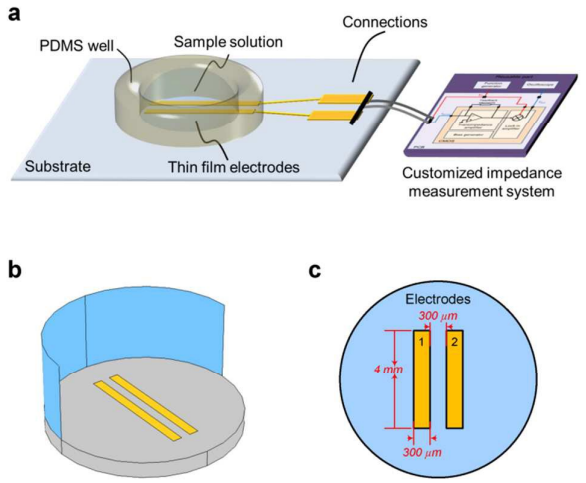

Fig. 1 (a) Schematic diagram of impedance measurement setup, thin-film electrodes with a customized impedance measurement system, (b) 3D view of the FEA simulation model, (c) topview of the model with dimensions.

electrodes is the cost, since most of nanomaterial fabrication and pattern involve expensive equipment and dedicated lab environments. In addition, high temperature and aggressive chemicals may also be involved, making most of these modified electrodes incompatible with cheap substrates, e.g. plastic and paper.

In this work, low-cost paper-based electrodes were applied to impedance measurements. The low-cost devices were directly printed by a standard office inkjet printer with commercial silver ink on glossy paper. As a control experiment, a group of printed electrodes was passivated with a layer of SiN_x to mimic the electrode-electrolyte double layer. Saline measurements were performed with both non-passivated and passivated Ag electrodes. Thin-film gold electrodes fabricated by conventional techniques were also used as a standard reference. From both saline measurements and simulation, the printed electrodes show an enhanced sensitivity over conventional thin-film gold electrodes.

2 Experimental

2.1 Electrode design and fabrication

2.1.1 Gold electrodes. Cr/Au (10 nm/90 nm) double layer metal films were deposited on glass substrate (Borofloat 33 glass from University Wafer) with a Lesker e-beam evaporator. Two 300 μm-width and 300 μm-separated electrodes were patterned with standard photolithography and lift-off methods with a film mask (JD Photo Data, UK). The gold electrodes are used as a reference for the contact and contactless inkjet-printed silver electrodes.

2.1.2 Inkjet-printed silver electrodes. 300 μm-width and 300 μm-separated electrodes patterns were designed with Microsoft Office Visio. Although one of the biggest features in inkjet printing is "pattern on demand", only parallel rectangular electrodes were printed in this work in order to match the dimension of the gold electrodes patterned via photolithography which were used as a reference. The electrodes were directly printed on HP advanced glossy photo paper with a Brother MFC-J6510DW office-used inkjet printer. All the colour cartridges were replaced with conductive silver ink from AgIC Inc. All designs were printed at A4 size and then cut into smaller pieces for measurements. One batch of printed electrodes was directly used to perform contact impedance measurement.

2.1.3 Inkjet-printed silver electrodes with passivation. One batch of printed silver electrodes was passivated with 200 nm SiN_x as an insulation layer to perform contactless impedance measurement. The insulation layer used here was to manipulate the electrode-electrolyte capacitance. The SiN_x layer was deposited with a cluster PECVD system (MVSystems LLC) at 150 °C substrate temperature.

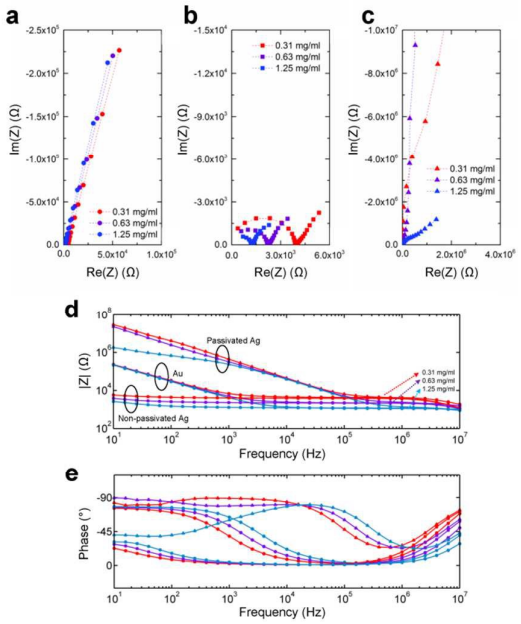

Fig. 2 (a) Cole-Cole pot of the measured impedance with different NaCl concentration using gold electrodes, (b) Cole-Cole pot of the measured impedance using non-passivated siliver electrodes, (c) Cole-Cole pot of the measured impedance using passivated electrodes, (d) merged results of all measurements.

View Article Online
DOI: 10.1039/C6RA18645A

2.2 Sodium chloride concentration measurements

Three groups of sodium chloride (NaCl) solution with different concentrations were prepared for the impedance measurements as shown in ESI table 1. The NaCl powder was purchased from Sigma-Aldrich (S7653). Deionised (DI) water from Sigma-Aldrich (38796) was used with conductivity lower than 4.3 µS/cm. 2.5 g of NaCl powder was dissolved in 1 L of DI water to prepare a stock solution at a concentration of 2.5 mg/ml. The stock solution was diluted with DI water by 1:1 yielding a concentration of 1.25 mg/ml, and further diluted for concentrations of 0.625 mg/ml and 0.312 mg/ml. 80 µl of each sample was used for each impedance measurements. As shown in Fig. 1a, all electrodes were surrounded by a PDMS ring to contain the electrolyte, and they were connected to an customized impedance measurement system[35]. An AC signal with the amplitude of 100 mV was used with the frequencies ranging from 10 Hz to 10 MHz. The measurement results were analysed and fitted with equivalent circuit models. All the data was fitted by ZView®, supplied by Scribner Associated Inc.

2.3 Finite element analysis

Finite element analysis (FEA) of the contact and contactless electrode systems was performed using COMSOL Multiphysics AC/DC package. A 3-dimensional model (as shown in Fig. 1b) was synthesised based on the specifications of the fabricated electrodes. Fig. 1c is the top view of the model, and the electrodes design is consistent with the dimensions of the fabricated electrodes. The model consists of an insulated substrate, conductive electrodes and electrolyte. For the contactless simulation, a thin dielectric layer was also inserted between electrodes and the electrolyte. The detailed simulation setup has been reported previously[36,37].

2.4 Cell constant analysis

The cell constant κ (cm^{-1}) was used in this study to evaluate the sensitivities of different electrodes. It can be calculated as[37]:

$$\kappa = |Z| \cdot \sqrt{\sigma^2 + \omega^2 \cdot {\varepsilon_0}^2 \cdot {\varepsilon_r}^2} \quad (1)$$

where $|Z|$ represents the magnitude of measured impedance, σ (mS/cm) is the conductivity of the electrolyte, ω is the angular frequency, ε_0 is the vacuum permittivity and ε_r the relative permittivity of the electrolyte.

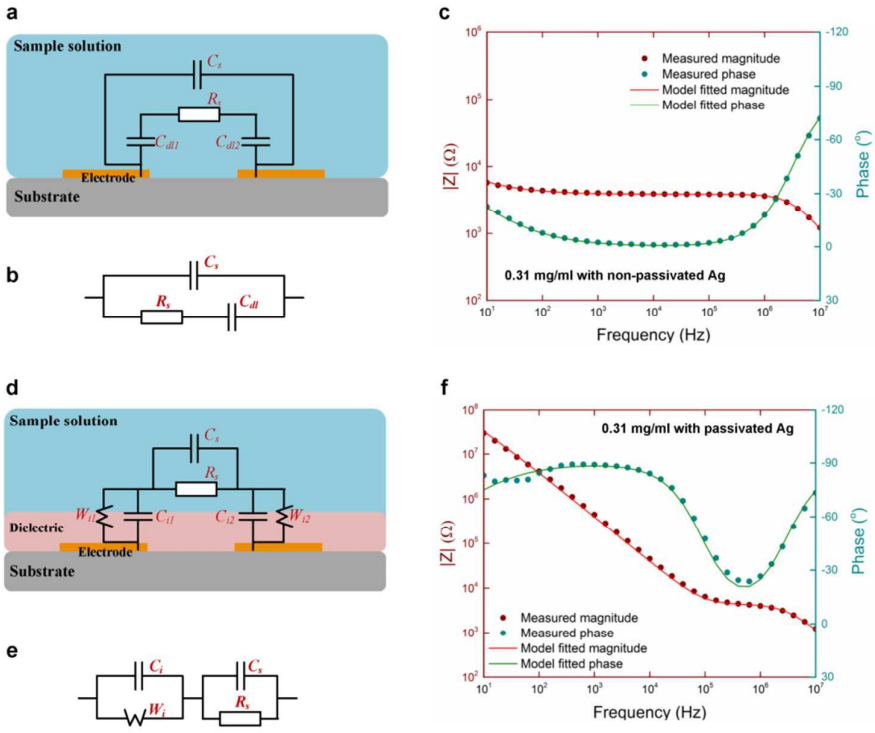

Fig. 3 (a) Schematics of impedance measurement with non-passivated electrodes, C_{dl} is the electrode-electrolyte double layer capacitance, R_s is the solution resistance and C_s is the solution capacitance; (b) simplified equivalent circuit model for non-passivated impedance measurement; (c) Bode plot of non-passivated Ag electrode measured and model fitted results by equivalent model in (b); (d) schematics of impedance measurement with passivated electrodes, the insulator capacitance C_i is used to replace the C_{dl}, warburg element W_i is used; (e) simplified equivalent circuit model for passivated impedance measurement; (f) Bode plot of passivated Ag electrode measured and model fitted results by equivalent model in (e).

View Article Online
DOI: 10.1039/C6RA18645A

3 Results and discussion

3.1 Sodium chloride concentration measurements

Three different concentrated NaCl solutions were measured by all three groups of electrodes. The Cole-Cole plots of the impedance measurements for Au, non-passivated and passivated Ag electrodes are shown as Fig. 2a, b and c. For Au electrodes (Fig. 2a) and non-passivated Ag electrodes (Fig. 2.b) measurements, higher concentration solution (data in blue) always shows lower impedance due to the higher solution conductivity. However, the passivated Ag electrodes (Fig. 2.c) measurements do not agree with the non-passivated

ones, indicating that the sample solutions were out of the sensitive region for the passivated Ag at part of the stimulus frequency. Figure 2d and e illustrate the Bode plot of all nine measurements. For Au electrodes, the constant slope at low frequency range (10 Hz to 10 kHz) for all three concentrations indicates the electrode-electrolyte double layer capacitance. As the measurement frequency increases, the influence of double layer capacitance reduces, and the magnitudes of impedance become independent of the stimulus frequency. The cut-off frequency (f_t) is defined as[38]:

$$f_t \approx \frac{1}{2\pi \cdot R_s \cdot C_{dl}} \quad (2)$$

where R_s is the solution resistance and the C_{dl} is the double layer capacitance. At the region ranging from 10 kHz to 5 MHz, the impedance magnitudes are distributed evenly according to the solution resistances. For the non-passivated Ag electrodes, the impedance magnitudes are independent of all measured frequencies. At lower frequencies (below 10 kHz), no clear capacitive behaviour is observed, and the phase elements (Fig. 2e) are staying nearly zero degree. The rough surface of the printed silver electrodes increases the effective electrode area significantly, and therefore the electrode-electrolyte double layer capacitance is increased. The cut-off frequency for non-passivated electrodes is lower than the minimum measured frequency (10 Hz) in this work. Above the Au electrode cut-off frequency (10 kHz), the measured impedance magnitudes are merged together with each saline concentration, reflecting the solution resistance (R_s).

For the passivated Ag electrodes, the electrolyte does not directly contact with the electrodes, and there is a layer of insulator performed as a dielectric layer. Therefore, the double-layer capacitance C_{dl} is replaced by the insulator capacitance C_i. In this work, a 200-nm SiN_x was used as the insulator, and the C_i is much smaller than C_{dl} in Au electrode since 200 nm is much greater than the typical dimension of the double layer. As a result, the cut-off frequency for passivated-Ag electrodes (Fig. 2.d) is much higher than that of Au electrodes.

3.2 Equivalent circuit fitting

Equivalent circuit models are used to further investigate the saline impedance results and validate the effects on double layer/insulator capacitances. As shown in Fig. 3a, a non-passivated impedance measurement model is presented, where C_{dl} is the double layer capacitance at both electrodes, R_s and C_s are the solution resistance and capacitance, respectively. Fig. 3b is the simplified model, which was used to fit all the non-passivated electrode measurements. Fig. 3c shows both the measured and modelled results of non-passivated Ag electrode in a Bode plot. Impedance magnitude and phase angle are all highly matched from 10 Hz to 10 MHz. Similar to the non-passivate ones, Fig. 3d shows the schematic of the model of passivated impedance measurement. Since glossy papers were used as the substrates and inkjet-printed Ag was used as the electrodes, the surface was too rough for the subsequence PECVD process to form an ideal insulation layer. Insulator capacitance (C_i) is paralleled with a Warburg element (W_i) to simulate the non-ideal interface and the dielectric leakage current induced resistance.

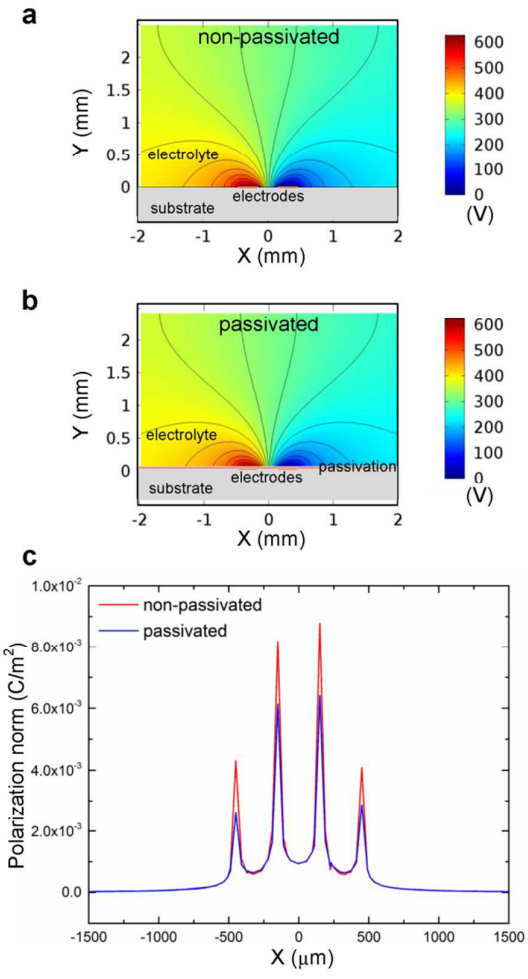

Fig. 4 FEA simulation results for non-passivated and passivated electrode arrangements. Cross-section electric potential distribution of the (a) non-passivated and (b) passivated electrode systems. The colour bar dnotes the potential strength in V. (c) Normalised polarisation over the interface.

View Article Online
DOI: 10.1039/C6RA18645A

Fig. 3e and f show the simplified equivalent circuit and the model fitted results. The fitting agreed with the measurement results over all frequencies. As shown in ESI Table 2, model extracted solution resistance (R_s) are consistent for all three groups of electrodes with the same sample concentration. Complete equivalent fitting results and parameters can be found in ESI Fig. 1-3.

3.3 FEA simulation

For impedance measurements, a source current was injected between the electrodes, leading to an electric field in the electrolyte. The electric potential distribution will affect the measurement results between different electrode setups. Therefore, it is important to understand the effect of the passivation layer on electric potential distribution to evaluate the electrode performance. Fig. 4a and b depict the potential distributions of non-passivated and passivated electrodes setup with 0.31 mg/ml NaCl solution. From the colour map and equal-potential lines, the two systems show identical results. Fig. 4c shows the normalized polarization at the interface. For the non-passivated model, the interface was defined as the top layer of the electrode, and the distance between the interface and the driving electrodes is zero. On the other hand, the passivated model defined the interface as the top of the insulation layer, and the gap between the interface and the electrodes is 200 nm. This difference causes the slight polarization mismatch as shown in Fig. 4c.

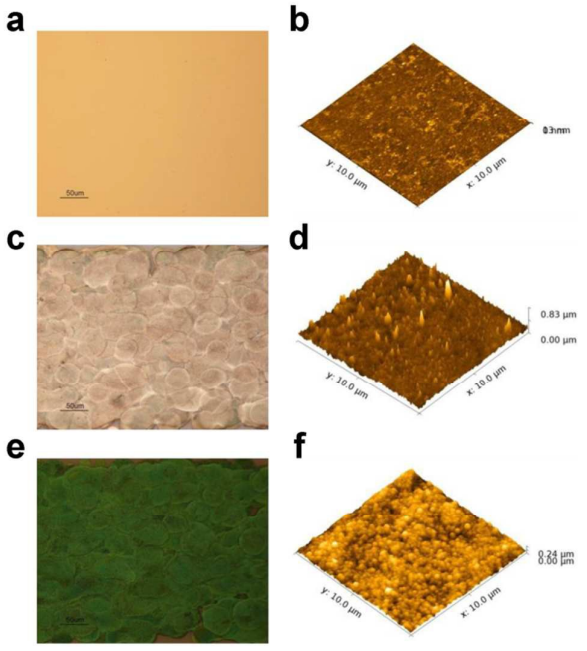

Fig. 5 Optical microscope images of (a) Au, (c) non-passivated Ag and (e) passivated Ag electrode surfaces; the scale bar is 50 µm. AFM images of (b) Au, (d) non-passivated Ag and (f) passivated Ag electrode surfaces over a 10 µm by 10 µm area.

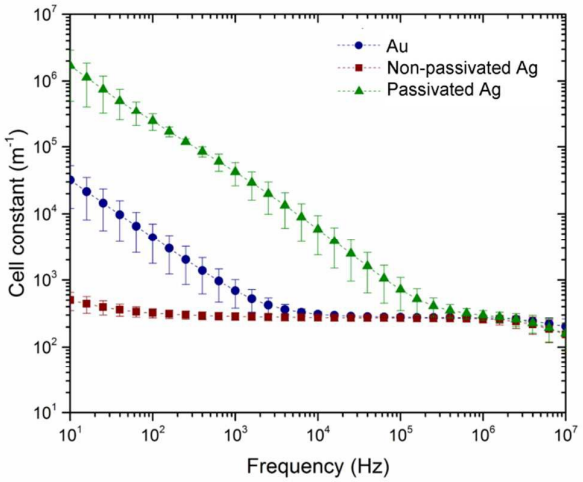

Fig. 6 Measured cell constants of Au, non-passivated and passivated Ag electrode systems. Errorbar shows the standard deviation over three different concentrated NaCl samples as a function of frequency.

3.4 Surface roughness

As discussed in section 3.1, the electrode surface roughness is the main reason for the increased double layer capacitance in non-passivated Ag electrodes. Figure 5.a shows an optical microscope image of the Au electrode surface, and Fig. 5.b is an AFM image over a 10 µm × 10 µm square. Vacuum deposition techniques normally give a very good film quality, and the RMS of this Au surface is only 0.8 nm. For the non-passivated Ag electrode, silver nanoparticles were directly inkjeted onto the substrate, and no post-annealing was applied. Ink droplets formed grains overlapped together, and the grain size as observed in Fig. 5c is about 50 µm. The AFM image (Fig. 5d) shows the surface roughness within one grain with 46.5 nm RMS. After passivated with SiN_x at 150 °C, the printed Ag was further sintered, and the grain size (Fig. 5e) was slightly increased. The AFM image of the insulator on the top of one grain is shown as Fig. 5f, and the RMS is approximately 26.4 nm.

3.5 Cell constant and sensitivity

The cell constant (as expressed in Eqn. 1) of an impedance sensor, is defined as the ratio of the measured impedance and the specific impedance of sample solution. It is an effective parameter to evaluate the electrode performance. In general, smaller cell constant indicate the sensor is more sensitive to the analyte.

Based on Eqn. 1 and parameters listed in ESI table 1, frequency-dependent complex domain cell constants of Au, non-passivated and passivated Ag electrodes were calculated. For each electrode system at a certain frequency, the mean cell constant value of three NaCl concentrations is plotted in Fig. 6 with the standard deviation as the error bar. The cut-off frequency of different electrodes is also reflected in this cell constant plot. For Au and passivated Ag electrodes, the cell constants reduce as the stimulus frequency increases, and it becomes frequency-independent after the cut-off point. Similar to the impedance Bode plot as shown in Fig. 2d, the

View Article Online
DOI: 10.1039/C6RA18645A

cut-off frequency of the non-passivated Ag is not observed in the measurement frequency range. The non-passivated Ag electrode cell constant remains at the lowest level from 10 Hz to 10 MHz. This reflects almost two-order sensitivity enhancement at 10 Hz. On the other hand, for the passivated Ag electrode, the electrode-electrolyte capacitance is artificially increased by an insulation layer. As a result the cell constant is more than an order of magnitude greater than that of the reference Au electrodes. This also explains why this electrode system is unlikely to be sensitive to any analyte in the lower frequency range, since the electrical double layer induced by the dielectric layer dominates the impedance measurement.

From the cell constant analysis, it is clear that a rough electrode surface produced by an office inkjet printer contributes to the reduction of electrode-electrolyte double layer impedance, thereby reducing the cell constant. Apart from electrode geometry optimization[39,40] and special measurement arrangement[37,41], electrode surface engineering can be considered as an alternative method to enhance the impedance sensing capability.

Conclusions

In this paper, low-cost electrodes were fabricated by a standard office inkjet printer with silver ink. This technique provides a 'pattern on demand' feature for electrodes fabrication, while significantly reduces the cost compared to lab-used material inkjet printer. In addition, the surface roughness of the printed silver electrodes is much higher compared to conventional thin-film gold electrodes; which significantly reduces electrode-electrolyte double layer impedance. It therefore leads to a reduced cell constant and a two-order sensitivity enhancement at 10 Hz. A separate experiment using passivated Ag electrode with SiN_x dielectric layer validate the theory that cell constant can be manipulated by controlling the electro-electrolyte double layer.

References

1 A. K. Yetisen, M. S. Akram and C. R. Lowe, *Lab Chip*, 2013, **13**, 2210–51.
2 C. Desmet, C. A. Marquette, L. J. Blum and B. Doumèche, *Biosens. Bioelectron.*, 2016, **76**, 145–163.
3 J. Hu, S. Wang, L. Wang, F. Li, B. Pingguan-Murphy, T. J. Lu and F. Xu, *Biosens. Bioelectron.*, 2014, **54**, 585–597.
4 J. Mettakoonpitak, K. Boehle, S. Nantaphol, P. Teengam, J. a. Adkins, M. Srisa-Art and C. S. Henry, *Electroanalysis*, 2016, **28**, 1-18.
5 N. K. Thom, G. G. Lewis, K. Yeung and S. T. Phillips, *RSC Adv.*, 2014, **4**, 1334–1340.
6 E. Petryayeva and W. R. Algar, *RSC Adv.*, 2015, **5**, 22256–22282.
7 W. Dungchai, O. Chailapakul and C. S. Henry, *Anal. Chem.*, 2009, **81**, 5821–5826.
8 M. Santhiago and L. T. Kubota, *Sensors Actuators, B Chem.*, 2013, **177**, 224–230.
9 Z. Nie, C. A. Nijhuis, J. Gong, X. Chen, A. Kumachev, A. W. Martinez, M. Narovlyansky and G. M. Whitesides, *Lab Chip*, 2010, **10**, 477–83.
10 D. L. Huber, R. P. Maginell, M. A. Samara, B.-I. Kim and B. C. Bunker, *Science (80-.).*, 2003, **301**, 352–354.
11 W. Gao, S. Emaminejad, H. Y. Y. Nyein, S. Challa, K. Chen, A. Peck, H. M. Fahad, H. Ota, H. Shiraki, D. Kiriya, D.-H. Lien, G. A. Brooks, R. W. Davis and A. Javey, *Nature*, 2016, **529**, 509–514.
12 U. Kim, S. Ghanbari, A. Ravikumar, J. Seubert and S. Figueira, *IEEE Trans. Eng. Heal. Med.*, 2013, **1**, 3700207–3700207.
13 I. Shitanda, M. Komoda, Y. Hoshi and M. Itagaki, *Analyst*, 2015, 6481–6484.
14 Z. Nie, F. Deiss, X. Liu, O. Akbulut and G. M. Whitesides, *Lab Chip*, 2010, **10**, 3163–3169.
15 L. Zhang, M. Zhou, D. Wen, L. Bai, B. Lou and S. Dong, *Biosens. Bioelectron.*, 2012, **35**, 155–159.
16 C. Sriprachuabwong, C. Karuwan, A. Wisitsorrat, D. Phokharatkul, T. Lomas, P. Sritongkham and A. Tuantranont, *J. Mater. Chem.*, 2012, **22**, 5478.
17 M. Singh, H. M. Haverinen, P. Dhagat and G. E. Jabbour, *Adv. Mater.*, 2010, **22**, 673–685.
18 H.-H. Lee, K.-S. Chou and K.-C. Huang, *Nanotechnology*, 2005, **16**, 2436–2441.
19 H. W. Choi, T. Zhou, M. Singh and G. E. Jabbour, *Nanoscale*, 2014, **7**, 3338–3355.
20 M. Crescentini, M. Bennati and M. Tartagni, *Electroanalysis*, 2012, **24**, 563–572.
21 H. Ma, R. W. R. Wallbank, R. Chaji, J. Li, Y. Suzuki, C. Jiggins and A. Nathan, *Sci. Rep.*, 2013, **3**, 2730.
22 J. Liu, S. Tian, P. E. Nielsen and W. Knoll, *Chem. Commun. (Camb).*, 2005, 2969–71.
23 K.-H. Lee, J.-O. Lee, M.-J. Sohn, B. Lee, S.-H. Choi, S. K. Kim, J.-B. Yoon and G.-H. Cho, *Biosens. Bioelectron.*, 2010, **26**, 1373–9.
24 M. S. Mannoor, T. James, D. V Ivanov, L. Beadling and W. Braunlin, *Biophys. J.*, 2010, **98**, 724–32.
25 S. K. Srivastava, R. Ramaneti, M. Roelse, H. D. Tong, E. X. Vrouwe, A. G. M. Brinkman, L. C. P. M. de Smet, C. J. M. van Rijn and M. a. Jongsma, *RSC Adv.*, 2015, **5**, 52563–52570.
26 T. Sun, E. J. Swindle, J. E. Collins, J. a Holloway, D. E. Davies and H. Morgan, *Lab Chip*, 2010, **10**, 1611–7.
27 R. Pradhan, S. Rajput, M. Mandal, A. Mitra and S. Das, *RSC Adv.*, 2014, **4**, 9432.
28 J. Chen, J. Cai, H. Hu, X. Huang, T. Yi, K. Wang and S. Pan, *RSC Adv.*, 2015, **5**, 85919–85927.
29 J. S. Daniels and N. Pourmand, *Electroanalysis*, 2007, **19**, 1239–1257.
30 B. J. Sanghavi, W. Varhue, J. L. Chávez, C. F. Chou and N. S. Swami, *Anal. Chem.*, 2014, **86**, 4120–4125.
31 M. a. Gross, M. J. a. Sales, M. a. G. Soler, M. a. Pereira-da-Silva, M. F. P. da Silva and L. G. Paterno, *RSC Adv.*, 2014, **4**, 17917.
32 Z. Wang, X. Zhou, J. Zhang, F. Boey and H. Zhang, *J. Phys.*

View Article Online
DOI: 10.1039/C6RA18645A

Chem. C, 2009, **113**, 14071–14075.
33 P. Alivisatos, *Nat. Biotechnol.*, 2004, **22**, 47–52.
34 P. Mostafalu and S. Sonkusale, *RSC Adv.*, 2015, **5**, 8680–8687.
35 H. Ma, J. Li, X. Cheng and A. Nathan, *Sensors Actuators B Chem.*, 2015, **211**, 77–82.
36 Y. Su, *Math. Probl. Eng.*, 2014, **2014**, e581063.
37 H. Ma, Y. Su and A. Nathan, *Sensors Actuators B Chem.*, 2015, **221**, 1264–1270.
38 B. Timmer, W. Sparreboom, W. Olthuis, P. Bergveld and A. van den Berg, *Lab Chip*, 2002, **2**, 121–4.
39 Q. Liu, J. Yu, L. Xiao, J. C. O. Tang, Y. Zhang, P. Wang and M. Yang, *Biosens. Bioelectron.*, 2009, **24**, 1305–10.
40 M. Varshney and Y. Li, *Biosens. Bioelectron.*, 2009, **24**, 2951–60.
41 V. Valente and A. Demosthenous, *Sensors*, 2016, **16**, 1159.

View Article Online
DOI: 10.1039/C6RA18645A

Table of contents entry

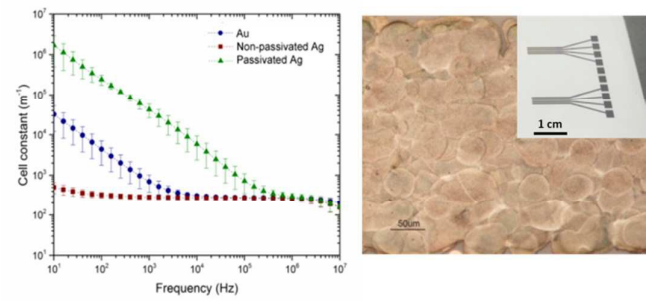

Paper electrodes, fabricated by a standard office inkjet printer, show a high sensitivity enhancement for impedance measurement.